batteries

Article

SOH Estimation Method for Lithium-Ion Batteries Using Partial Discharge Curves Based on CGKAN

Shengfeng He [1], Wenhu Qin [1,*], Zhonghua Yun [2], Chao Wu [1] and Chongbin Sun [1]

[1] School of Instrument Science and Engineering, Southeast University, No. 2 Sipailou, Nanjing 210096, China; heshengfeng@seu.edu.cn (S.H.); chaowu@seu.edu.cn (C.W.); sunchongbin@seu.edu.cn (C.S.)
[2] School of Intelligent Science and Technology, Xinjiang University, No. 777 Huarui Road, Urumqi 830046, China; zhonghuayun@xju.edu.cn
* Correspondence: qinwenhu@seu.edu.cn

Abstract: Accurate estimation of the state of health (SOH) of lithium-ion batteries is essential to ensure the safe and stable operation of equipment such as electric vehicles. To address the limitations in the accuracy and robustness of existing methods under complex operating conditions, a CNN-BiGRU-KAN (CGKAN) method for SOH estimation based on partial discharge curves is proposed. Firstly, random forest analysis is applied to extract features highly correlated with battery health from the partial discharge curve data. Next, a SOH estimation framework based on the CGKAN model is developed, where 1-Dimensional-Convolutional Neural Networks (1D-CNN) are used to extract deep features from the original data, Bidirectional Gated Recurrent Unit (BiGRU) captures the bidirectional dependencies of the time series, and Kolmogorov–Arnold Networks (KAN) enhances the modeling of complex nonlinear features through its nonlinear mapping capabilities, thereby improving the accuracy of SOH estimation. Finally, multiple experiments under different conditions are conducted, and the results demonstrate that the proposed CGKAN method, by integrating the individual advantages of 1D-CNN, BiGRU, and KAN, efficiently captures complex nonlinear patterns in battery health features and maintains stable performance across various operating conditions.

Keywords: state of health; random forest; BiGRU; KAN; CGKAN

check for updates

Academic Editor: Odne S. Burheim

Received: 14 February 2025
Revised: 26 March 2025
Accepted: 22 April 2025
Published: 23 April 2025

Citation: He, S.; Qin, W.; Yun, Z.; Wu, C.; Sun, C. SOH Estimation Method for Lithium-Ion Batteries Using Partial Discharge Curves Based on CGKAN. *Batteries* **2025**, *11*, 167. https://doi.org/10.3390/batteries11050167

Copyright: © 2025 by the authors. Licensee MDPI, Basel, Switzerland. This article is an open access article distributed under the terms and conditions of the Creative Commons Attribution (CC BY) license (https://creativecommons.org/licenses/by/4.0/).

1. Introduction

Lithium-ion batteries, with advantages such as high energy density, long cycle life, and wide operational temperature range, are currently the primary energy storage choice for electric vehicles [1,2]. However, during charging and discharging cycles, the available capacity of lithium-ion batteries decreases, which undermines the reliability of the equipment during operation [3]. Therefore, accurately and effectively estimating the state of health (SOH) of lithium-ion batteries has become a critical task for battery management systems (BMS) [4]. SOH reflects the degree of battery aging and is of vital importance for ensuring the safety of electric vehicles. The SOH of a battery is typically expressed as the ratio of the current maximum capacity (C_i) to the nominal capacity (C_o), represented as $SOH = C_i/C_o \times 100\%$. However, due to the strong nonlinear characteristics of lithium-ion batteries, directly measuring SOH is challenging. Currently, common methods for estimating SOH are mainly divided into model-based and data-driven approaches [5].

Model-based methods primarily rely on electrochemical models [6] and equivalent circuit models [7] to construct mathematical degradation models of lithium-ion batteries. Electrochemical models, which are based on electrochemical kinetics, extract internal parameters that represent the battery aging process to build models for SOH estimation [8]. Xiong et al. [9] developed an electrochemical model based on electrochemical theory, extracting five aging feature parameters highly correlated with battery degradation, and used these parameters to describe the degradation trajectory of SOH. Deng et al. [10] proposed a reduced-order electrochemical model for all-solid-state batteries, achieving a trade-off between model fidelity and computational complexity, making it suitable for integration into BMS. In contrast, equivalent circuit models mainly study the electrical characteristics of battery aging and require fewer computational resources compared to electrochemical models. Galeotti et al. [11] presented an equivalent circuit model based on electrochemical impedance spectroscopy and utilized the correlation between ECM parameters and SOH for accurate SOH estimation. Hu et al. [12] proposed a collaborative SOH estimation scheme based on fractional-order models, which maintains SOH estimation stability even in the presence of initial bias, noise, and disturbances. Model-based methods offer strong interpretability but require substantial prior knowledge of battery aging mechanisms, and their accuracy and robustness may be affected in complex operating scenarios [13,14].

In recent years, data-driven methods have rapidly developed and found widespread application in SOH estimation due to their self-learning capabilities and nonlinear mapping ability [15]. Data-driven approaches typically consist of two stages: feature extraction and model construction. The first stage involves extracting health features that are highly correlated with battery degradation from aging data. Health features are classified into direct and indirect health features. Direct health features are extracted directly from charging voltage or current without the need for additional data transformation. Gou et al. [16] extracted duration of the same voltage range from charging data as a key health feature from charging data, using Pearson correlation analysis to select the four most optimal features as inputs to the model. Teng et al. [17] utilized discharge information from retired batteries to extract multiple features, such as voltage difference, voltage change rate, and voltage deviation rate, from voltage data at equal time intervals. Pan et al. [18] studied the relationship between internal resistance variation and capacity degradation, extracting increments in ohmic internal resistance and polarized internal resistance as features. Zhu et al. [19] extracted six statistical features based on the relaxation voltage curve after full charging and statistical methods, which effectively describe the capacity degradation of lithium-ion batteries. Indirect health features are obtained through transformation of voltage or temperature data. Weng et al. [20] applied incremental capacity analysis to convert the charging voltage curve into a V–Q curve and extracted features based on changes in the curve peaks. Wang et al. [21] constructed a differential thermal voltammetry curve based on voltage and temperature data, from which features such as peak position, peak value, and valley value were extracted.

The second stage involves constructing the SOH estimation model, which establishes a mapping from health features to SOH. Data-driven SOH estimation models are primarily divided into two categories: shallow machine learning models and deep learning models. For example, Wu et al. [22] proposed an SOH estimation method based on particle swarm optimization combined with a backpropagation neural network, where PSO is used to optimize the weights of BPNN for accurate SOH estimation. Yun et al. [23] introduced a least squares support vector machine to build a nonlinear SOH prediction model and validated the model's accuracy using the CALCE dataset. However, machine learning models tend to overfit or perform poorly when there is insufficient data or inadequate feature

representation, and they struggle to capture the multimodal data of lithium-ion batteries (e.g., the coupling relationships between voltage, temperature, and internal resistance). As a result, many researchers have adopted deep learning methods for SOH estimation. Yang et al. [24] proposed a random forest-convolutional neural network (RF-CNN) SOH model, where CNN is used to estimate both SOH and its increment, and the random forest method is employed to fuse the results for SOH estimation. Zheng et al. [25] noted that CNNs cannot capture the time-based features of sequences and thus proposed a convolutional Gated Recurrent Unit (CNN-GRU) model for SOH estimation during the random charging process of lithium-ion batteries. This model utilizes CNN to explore the intrinsic relationships in the data and leverages the temporal memory capability of GRU to learn the dynamic changes within the data. Wang et al. [26] addressed both model training time and prediction accuracy by decomposing SOH using empirical mode decomposition, obtaining intrinsic mode function components and residual signals, and employing GRU to predict the high-frequency components of SOH, while using a random forest model to predict the residual components, ultimately achieving SOH estimation.

From the research of many scholars, it is evident that data-driven methods for SOH estimation of lithium-ion batteries currently face several challenges. First, health feature extraction typically requires complete charge and discharge cycle data, but it is often difficult to collect such comprehensive data under real-world constraints. Second, the ability of models to capture the bidirectional dependencies inherent in time-series data is often weak. Third, when faced with high-dimensional complex nonlinear mappings, models require a large number of hidden layers and nodes to approximate the target function, leading to a massive increase in model parameters and a decrease in training efficiency. Moreover, the battery capacity degradation process is highly correlated with operating conditions, and the lack of model generalization leads to suboptimal SOH estimation under complex operating scenarios. To address these issues, this paper proposes a CNN-BiGRU-KAN (CGKAN) method for SOH estimation based on partial discharge curves. First, direct health feature and indirect health features are extracted from partial discharge curves based on the state of charge intervals, with feature importance assessment and selection performed using random forest. Then, CNN is used to extract local features, BiGRU captures both forward and backward information, and KAN's nonlinear fitting is employed for SOH estimation. Finally, SOH estimation experiments are conducted using 12 batteries from the NASA and CALCE datasets. The results show that the proposed method achieves high SOH estimation accuracy and is capable of adapting to different types of lithium-ion batteries and operating conditions.

The remainder of this paper is organized as follows: Section 2 presents the extraction of health features from partial discharge curves of the battery, along with feature analysis and selection using random forest. Section 3 details the construction of the CNN-BiGRU-KAN model for SOH estimation of lithium-ion batteries. Section 4 presents SOH estimation experiments under different conditions, followed by analysis and discussion. Finally, Section 5 concludes this paper.

2. Health Feature Analysis and Construction

2.1. Battery Degradation Data Analysis

In this paper, this study initially involved four batteries (B05, B06, B07, B18) from the NASA dataset, each with 2 Ah capacity. These batteries underwent charging at 1.5 A constant current until reaching 4.2 V at 24 °C, followed by constant voltage charging until current decreased to 20 mA. During the discharging phase, the respective cutoff voltages were set as follows: B05 at 2.7 V, B06 at 2.5 V, B07 at 2.2 V, and B18 at 2.5 V under 2 A constant current discharge. To analyze temperature and discharge rate effects,

additional batteries B34, B45 and B55 were included. The CALCE dataset comprised CS2_35-CS2_38 batteries (1.1 Ah capacity) with identical charging protocol (0.55 A constant current to 4.2 V then constant voltage to 20 mA), discharged at 1.1 A until reaching 2.7 V cutoff [27–30]. The detailed experimental parameters is shown in Table 1. Figure 1a,b illustrate the capacity degradation processes of lithium batteries under mild and complex operating conditions, respectively, as derived from the NASA dataset, while Figure 1c presents the degradation process from the CALCE dataset. It is apparent that, with an increasing number of cycles, internal components of the battery—such as the electrodes and electrolyte—gradually undergo aging, leading to a decline in capacity and a subsequent deterioration of the SOH. However, this degradation process is intermittently accompanied by irregular capacity increases, which poses a significant challenge for SOH estimation research.

Table 1. Experimental conditions for each battery.

Battery	°C	Charging (A)	Cutoff (V)	Discharging (A)	Cutoff (V)
B05, B06, B07, B18	24	1.5	4.2	2.0	2.7, 2.5, 2.2, 2.5
B34, B45, B55	24, 4, 4	1.5	4.2	4.0, 1.0, 2.0	2.2, 2.0, 2.5
CS2_35, CS2_36, CS2_37, CS2_38	\	0.55	4.2	1.1	2.7

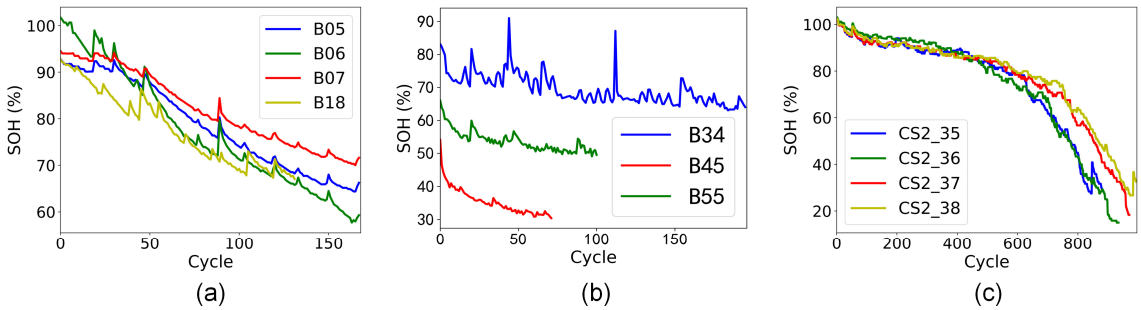


Figure 1. Degradation curve: (**a**) NASA mild; (**b**) NASA complex; (**c**) CALCE.

2.2. Health Feature Construction Based on Partial Discharge Curves

Since it is challenging to utilize information related to the entire battery discharge process under various practical application constraints, the SOC of a battery, which refers to the ratio of the current remaining capacity to the nominal capacity, is typically in the range of 80% to 20% during use [31]. Therefore, to reduce the model's dependence on data completeness, this paper investigates and constructs the health features of the battery by segmenting the discharge curve based on this range of SOC intervals.

Accurate SOC is difficult to measure directly, previous research indicates that the battery terminal voltage decreases as the SOC declines, meaning that the battery terminal voltage can be considered as an external representation of its SOC [32]. As shown in Figure 2 for battery B05, the SOC–voltage relationship curve indicates that the maximum voltage corresponding to 80% SOC is approximately 3.75 V, while the minimum voltage corresponding to 20% SOC is approximately 3.25 V. Therefore, this paper selects the voltage range from 3.25 V to 3.75 V for feature extraction.

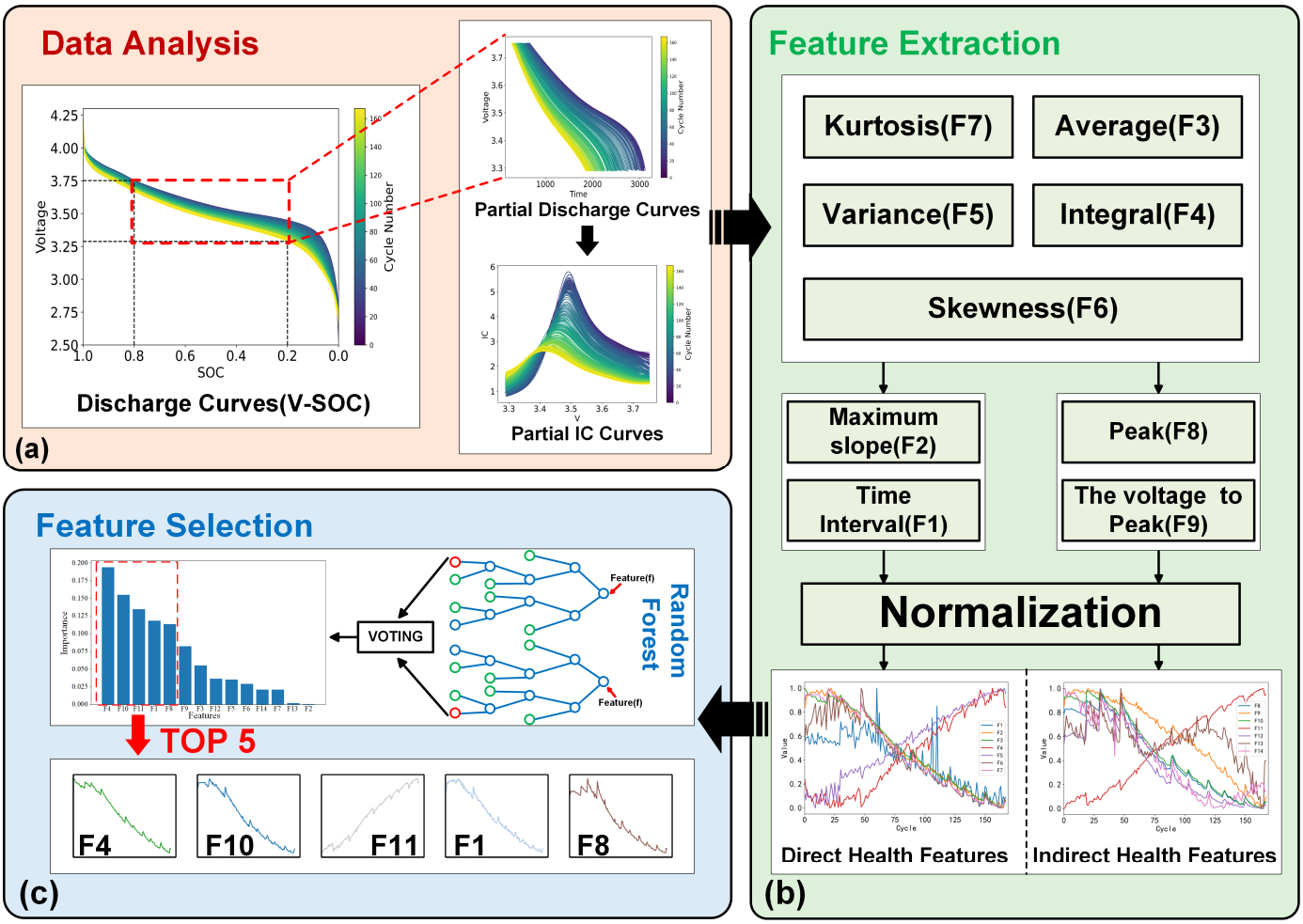


Figure 2. Data processing (B05): (**a**) data analysis; (**b**) feature extraction; (**c**) feature selection.

2.2.1. Feature Extraction Based on Voltage Curve

The voltage curve of the battery from 3.75 V to 3.25 V is shown in Figure 2a. As observed, with the use of charging and discharging cycles, the voltage curve gradually shifts to the left. Therefore, the degradation trend of the battery can be described using the maximum slope of the voltage curve, the average voltage, the integral of the voltage curve with respect to time, the voltage variance, skewness, and kurtosis. Additionally, because the linearity of the voltage drop from 3.7 V to 3.5 V is high in the figure, the time interval of this voltage range can also be used as a health feature. The construction methods for each health feature are as follows:

$$\mathrm{F1} = t_{3.7} - t_{3.5} \tag{1}$$

$$\mathrm{F2} = \max\left(\frac{V_{t+\Delta t} - V_t}{\Delta t}\right) \tag{2}$$

$$\mathrm{F3} = \overline{V} = \frac{\sum_{i=1}^{N} V_i}{N} \tag{3}$$

$$\mathrm{F4} = \int \mathrm{V}\ \mathrm{dt} \tag{4}$$

$$\mathrm{F5} = \frac{\sum_{i=1}^{N} \left(V_i - \overline{V}\right)^2}{N} \tag{5}$$

$$\mathrm{F6} = \frac{\frac{1}{N}\sum_{i=1}^{N} \left(V_i - \overline{V}\right)^3}{\left(\frac{1}{N}\sum_{i=1}^{N} \left(V_i - \overline{V}\right)^2\right)^{3/2}} \tag{6}$$

$$\mathrm{F7} = \frac{\frac{1}{N}\sum_{i=1}^{N}\left(V_i - \overline{V}\right)^4}{\left(\frac{1}{N}\sum_{i=1}^{N}\left(V_i - \overline{V}\right)^2\right)^2} - 3 \tag{7}$$

where N is the total number of voltage samples, and V_i is the i-th voltage value. $t_{3.7}$ and $t_{3.5}$ are the times when the voltage drops to 3.7 V and 3.5 V, respectively. Due to the differences in magnitude of these features, excessively large or small eigenvalues can affect the convergence speed and accuracy of the SOH estimation model. Therefore, the health features F1 to F7 are normalized as shown in Equation (8):

$$X_{\mathrm{scaled}} = \frac{X - X_{\min}}{X_{\max} - X_{\min}} \tag{8}$$

where X is the original feature value, X_{scaled} is the scaled feature value, $X_{\min}$ is the minimum value of the feature, and $X_{\max}$ is the maximum value of the feature. The normalized features are shown in Figure 2b.

2.2.2. Feature Extraction Based on the IC Curve

Incremental capacity analysis analyzes the phase transition characteristics and aging mechanisms of the battery at the electrode level. This method converts the battery's voltage plateau into clearly identifiable peaks on the IC curve, from which features are indirectly extracted to characterize the battery's aging state [33]. In CC discharge mode, the IC is defined as:

$$IC = \frac{dQ}{dV} = I \cdot \frac{dt}{dV} \tag{9}$$

where Q is the capacity, V is the voltage, and t is the sampling time. The original IC curve usually contains a lot of noise, so Gaussian filtering is applied to smooth the IC curve, making each peak of the IC curve clearly visible. As an example, the IC curve after dividing the SOC range of (80%, 20%) for B05 is shown in Figure 2a.

As seen in Figure 2a, with the battery charging and discharging cycles, the battery capacity gradually declines, the IC curve flattens, and its peak diminishes, with the corresponding peak voltage also decreasing. These changes in the curve's position and shape reflect the internal aging mechanisms of the battery. Therefore, the following health features are constructed: the peak value of the IC curve (F8), and the voltage corresponding to the peak (F9). The principles for constructing features F10–F14 are the same as for F2–F6 in Section 2.2.1. The methods for constructing F8 and F9 are as follows:

$$\mathrm{F8} = \max(IC) \tag{10}$$

$$\mathrm{F9} = V_{IC=\max(IC)} \tag{11}$$

After normalizing the data for the indirect health features constructed for the B05 battery as in Equation (8), as shown in Figure 2b, it can be observed that features F8, F9, F10, F12, F13, and F14 show a decreasing trend, which is positively correlated with SOH degradation, while feature F11 shows an increasing trend, which is negatively correlated with SOH degradation.

2.3. Health Feature Analysis Based on Random Forest Regression

It can be intuitively seen that various features do not characterize SOH to the same extent, and thus correlation analysis of the 14 extracted health features is required. Common correlation analysis methods include Pearson and Spearman, but these methods perform poorly in handling nonlinear relationships and are sensitive to outliers [34]. Additionally, there is autocorrelation among the health features, which can lead to feature redundancy. Random forest regression [35] is an ensemble learning algorithm based on independent

decision trees as base learners. Random forest regression builds multiple decision trees using random sampling and random feature selection, where each tree is trained on different data subsets and feature subsets. The final prediction result is obtained by aggregating the predicted values from each tree through voting and averaging.

In feature analysis based on random forest regression, the importance of a feature is evaluated by randomly shuffling its values and observing its impact on the model's performance. The specific steps are as follows:

(1) For the original data D, the random forest regression model accuracy err_{orig}, represented here by the mean square error (MSE), is calculated as follows:

$$MSE = \frac{1}{N}\Sigma_{i=1}^{N}(\hat{y}_i - y_i)^2 \quad (12)$$

where $\hat{y}_i$ and y_i are the estimated and actual values of SOH for the i-th sample, respectively, and N is the number of samples.

(2) To reduce the chance error caused by randomly replacing features, the following steps are repeated K times (with K set to 5 in our experiments): replace the features F_j and record the newly generated dataset as $D_{k,j}$ $(k = 1, 2, \ldots K)$; recalculate the model's accuracy $err_{k,j}$ for the new dataset $D_{k,j}$.

(3) Calculate the feature importance δ_j for feature j:

$$\delta_j = \frac{1}{K}\Sigma_{k=1}^{K} err_{k,j} - err_{orig} \quad (13)$$

(4) After obtaining the importance of all the features, the data is normalized to obtain the final importance as follows:

$$Importance_j = \frac{\delta_j}{\Sigma_{j=1}^{14}\delta_j} \quad (14)$$

The importance of each feature of the normalized B05 is depicted in Figure 2c, where a larger value indicates a stronger correlation between the feature and SOH. Notably, the importance of features F4, F10, F11, F1, and F8 in the figure is greater than 0.1, while the importance of the other features is less than or equal to 0.08. Therefore, these five features are considered as the key features for determining the SOH of B05 battery. In addition, the problem of multicollinearity among features was addressed by computing the Pearson and Spearman correlation coefficient matrices of the selected features after each round of feature selection, ensuring that no pair of variables was found to exhibit a strong correlation.

3. Method

This paper proposes a model that combines 1D-CNN, BiGRU, and KAN for estimating battery SOH. The 1D-CNN extracts deep features from original data, BiGRU captures the bidirectional dependencies of the time series, and KAN enhances the modeling of complex nonlinear features to further improve the accuracy of health state estimation.

3.1. 1D-CNN

Convolutional Neural Networks (CNNs) are widely used in image recognition and processing. In image recognition, CNNs typically use 2D convolutional kernels to extract spatial features. However, in SOH estimation, the input features are time-dependent time-series data, and traditional 2D convolutional kernels are not suitable. Therefore, a 1D convolutional kernel is employed to leverage the CNN's superior ability to extract local features.

The 1D-CNN architecture used in this paper is shown in Figure 3. A 2D-CNN extracts pixel features from local regions through convolution in the spatial dimension, while a 1D-CNN extracts key trends and patterns from the time series by convolving along the temporal dimension. Specifically, in the 1D-CNN used in this paper, the convolutional layers identify fluctuations in the battery's current and voltage, as well as temperature variations in the NASA dataset, to help the model capture potential patterns of battery performance degradation. The activation layer uses ReLU as the activation function, allowing the model to learn complex patterns of battery health state changes, rather than simply linearly combining features. The max-pooling layer is used for down-sampling, which helps reduce computational complexity and extracts the most important features, thereby preventing model overfitting.

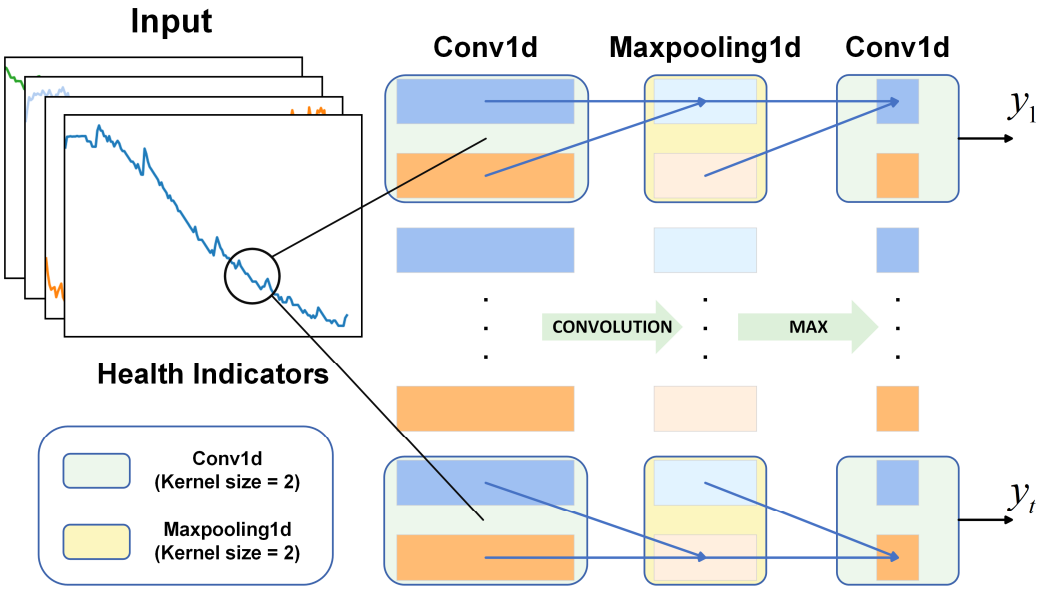


Figure 3. 1D-CNN structure.

3.2. BiGRU

The Gated Recurrent Units (GRU) aims to address the vanishing gradient problem in simple RNNs by incorporating gating mechanisms. Unlike LSTM, GRU reduces the three gates in LSTM to two gates: the reset gate and the update gate. Additionally, GRU eliminates the cell state component present in LSTM, making it an improved version of the LSTM network.

The internal structure of GRU is shown in Figure 4c. It can be observed that the update gate (z_t) in GRU is responsible for updating the hidden state. The input vector (x_t) and the previous hidden state (h_{t-1}) pass through the Sigmoid function to generate the update gate, represented by Equation (15):

$$z_t = \sigma(W_z \cdot [h_{t-1}, x_t] + b_z) \tag{15}$$

where σ represents the Sigmoid activation function, and the output value lies between 0 and 1. W_z is the weight matrix for the update gate, and b_z is the bias matrix for the update gate. The reset gate (r_t) controls how much historical information should be ignored, as described by:

$$r_t = \sigma(W_r \cdot [h_{t-1}, x_t] + b_r) \tag{16}$$

where W_r is the weight matrix for the reset gate, and b_r is the bias matrix for the reset gate. The output of the reset gate is multiplied with the hidden state, and the input vector is

added to it. This result is then passed through the tanh function to obtain the new memory content, represented by Equation (17):

$$\tilde{h}_t = \tanh(\mathrm{W_h}\cdot[r_t \times h_{t-1}, x_t] + b_h) \tag{17}$$

where W_h and b_h are the weight matrix and the bias matrix of the new memory cell state, respectively. Once the memory content is obtained, the output of the current neuron is derived using Equation (18):

$$h_t = (1 - z_t) \times h_{t-1} + z_t \times \tilde{h}_t \tag{18}$$

Since GRU efficiently extracts time-series features related to battery performance degradation, it can only capture forward temporal sequence information while neglecting backward information. However, backward information often contains feedback effects of degradation processes that occur during battery use, including capacity growth, internal resistance changes. These factors typically manifest in the later stages of the battery's charge and discharge cycles and directly affect the battery's health state. To address this issue, a bidirectional GRU (BiGRU) model is introduced, which processes the time-series data through both forward and backward layers. This allows the model to capture both past and future degradation trends in the battery's health state.

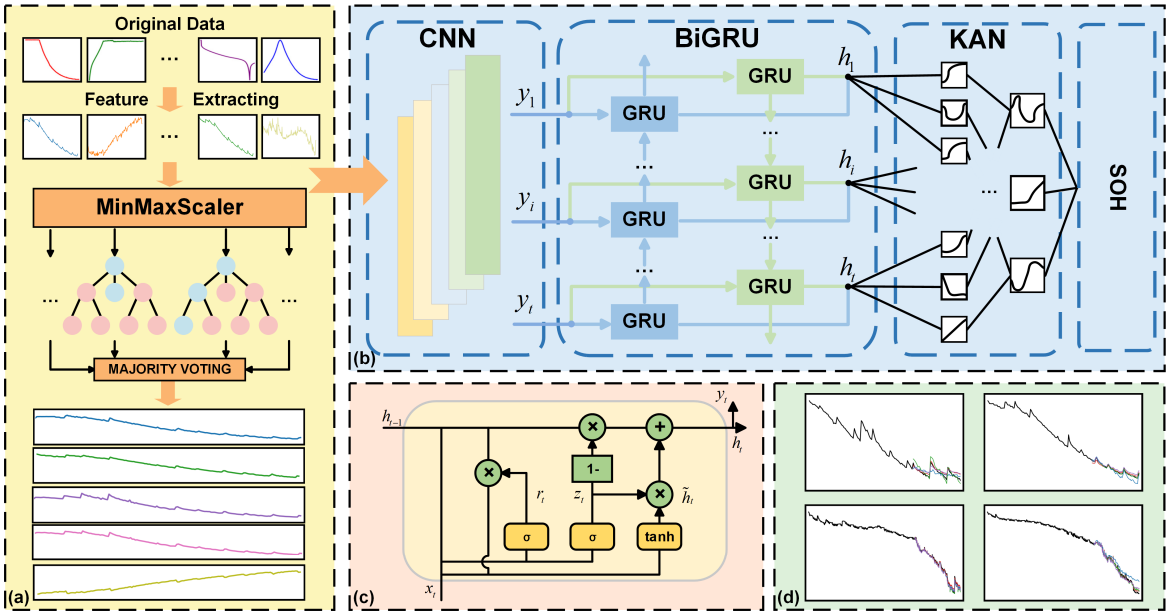


Figure 4. The framework based on CGKAN method: (**a**) feature extraction and selection; (**b**) CGKAN model; (**c**) GRU detailed structure; (**d**) SOH estimation results.

3.3. KAN

Kolmogorov–Arnold Networks (KAN) is a novel neural network architecture based on the Kolmogorov–Arnold representation theorem. In recent years, KAN has gained increasing attention for its powerful approximation capabilities, and has been successfully applied in various fields such as image classification [36], time-series prediction [37].

Unlike traditional neural networks, KAN employs learnable activation functions, allowing each weight parameter to be substituted by a univariate function, thus enhancing the model's flexibility and parameter efficiency. KAN is capable of dynamically adjusting to extract nonlinear features from data, making it particularly suitable for handling complex patterns in battery data.

According to the Kolmogorov–Arnold superposition theorem, any multivariate continuous function on a bounded domain can be represented as a finite sum of univariate functions. Therefore, a smooth and continuous multivariate function $f(\boldsymbol{x}) : [0,1]^n \to \mathbb{R}$ can be represented by a finite sum of univariate functions [38]:

$$f(\boldsymbol{x}) = \sum_{i=1}^{2n+1} \Phi_i \left(\sum_{j=1}^{n} \phi_{i,j}(x_j) \right) \tag{19}$$

where $\boldsymbol{x} = [x_1, x_2, \cdots, x_n]$ is input, and $\Phi_i : \mathbb{R} \to \mathbb{R}$ and $\phi_{i,j} : [0,1] \to \mathbb{R}$ represent the external and internal functions, respectively. This structure simplifies high-dimensional function learning tasks into the learning of multiple univariate functions.

Equation (19) contains 2 nonlinear layers and $2n+1$ intermediate layers, using B-spline functions as Φ_i and $\phi_{i,j}$ to approximate the target function. The spline functions, defined by control points, create smooth curves for interpolation or approximation of data features in battery SOH estimation. The order of the spline function $k(k = 3)$ determines the degree of the polynomial connecting the control points, while the number of intervals G defines the number of segments between the control points. This enables the spline functions to accurately capture subtle variations in the battery degradation process.

In Equation (19), the network is represented by a two-layer structure, where the activation functions are positioned at the edges, and the nodes perform summation. This structure simplifies computations, but it is challenging to effectively approximate complex battery degradation characteristics, such as capacity loss or increased internal resistance, with high precision. Therefore, a wider and deeper KAN network architecture is required to better capture the complex nonlinear features in the battery health state.

The KAN layer is defined by the matrix $\boldsymbol{\Phi}$ [39], which consists of univariate functions $\{\phi_{i,j}(\cdot)\}$, where $i = 1, \cdots N_{in}$ and $j = 1, \cdots N_{out}$, N_{in} and N_{out} represent the number of inputs and outputs, respectively, and $\phi_{i,j}$ are the aforementioned trainable spline functions. It is noted that, according to Equation (19), the Kolmogorov–Arnold representation theorem can be expressed as two-layer KANs. The internal functions form a KAN layer with $N_{in} = n$ and $N_{out} = 2n+1$, while the external functions form another KAN layer with $N_{in} = 2n+1$ and $N_{out} = 1$.

The shape of the KAN can be described using $[n_1, \cdots n_{L+1}]$, where L represents the number of layers in the KAN. The KAN defined by the Kolmogorov–Arnold theorem has the shape $[n, 2n+1, 1]$, which represents the shallow KAN structure. A generally deeper KAN can be represented by the composition of L layers:

$$\boldsymbol{y} = KAN(\boldsymbol{x}) = (\boldsymbol{\Phi}_{\mathrm{L}} \circ \boldsymbol{\Phi}_{\mathrm{L}-1} \circ \cdots \circ \boldsymbol{\Phi}_1)\boldsymbol{x} \tag{20}$$

Spline functions are used for precise modeling of low-dimensional battery health state features, while Multi-Layer Perceptrons (MLPs) efficiently handle high-dimensional degradation features. By combining the advantages of spline functions and MLPs, KAN can accurately extract key features, such as charging/discharging patterns and fluctuations in current and voltage, from low-dimensional data. Simultaneously, in the high-dimensional feature space, it optimizes complex degradation patterns, thereby enhancing the precision and robustness of SOH estimation.

3.4. CGKAN

Step 1: Data Analysis and Feature Extraction. Analyze battery aging data to systematically derive health features and construct a structured dataset that links key features to corresponding SOH values.

Step 2: Feature Analysis and Selection. Use random forest regression to rank the health features by importance and select the top five features as inputs for the CGKAN model.

Step 3: CNN-Based Feature Extraction. Employ a 1D-CNN to process the input data, extract local features, and capture temporal dependencies through convolutional layers, generating feature maps for SOH estimation.

Step 4: BiGRU Temporal Modeling. Feed the features extracted by the CNN into a BiGRU network to capture bidirectional temporal dependencies in the time-series data.

Step 5: KAN Nonlinear Optimization. Apply KAN to perform nonlinear optimization, refining the feature representations from the BiGRU to improve estimation accuracy.

4. Experiments and Analysis

4.1. SOH Estimation Accuracy Experiment

To validate the estimation accuracy of the proposed method on future cycle data of batteries, experiments were conducted on NASA (B05, B06, B07, B18) and CALCE (CS2_35, CS2_36, CS2_37, CS2_38) datasets. The first 70% of each battery's cycle data was used for training, with the remainder for testing. Comparative experiments with CNN, BiGRU, and CNN-BiGRU (using an MLP as the final regression layer) were also performed. Three error metrics—mean absolute error (MAE), root mean square error (RMSE), and mean absolute percentage error (MAPE)—were used for evaluation, with their formulas as follows:

$$MAE = \frac{1}{N}\Sigma_{i=1}^{N}|y_i - \hat{y}_i| \times 100\% \tag{21}$$

$$RMSE = \sqrt{\frac{1}{N}\Sigma_{i=1}^{N}(y_i - \hat{y}_i)^2} \times 100\% \tag{22}$$

$$MAPE = \frac{1}{N}\Sigma_{i=1}^{N}\left|\frac{y_i - \hat{y}_i}{y_i}\right| \times 100\% \tag{23}$$

where y_i and $\hat{y}_i$ represent the actual value and estimated value of the i-th sample, respectively, and N is the number of samples. The estimation results and evaluation results for the NASA dataset are shown in Figure 5 and Table 2, while the estimation results and evaluation results for the CALCE dataset are shown in Figure 6 and Table 3.

As shown in Figure 5, the CGKAN method effectively fits the SOH degradation curves for B05, B06, B07, and B18. With the exception of a few instances in the capacity regeneration region and the latter stages of degradation in the test data, the errors for most of the test points are within 1%. Therefore, this method can accurately describe the trend of capacity degradation and effectively capture the capacity regeneration phenomenon.

Table 2. Evaluation metrics of ablation settings and initialization cycles on the NASA dataset.

No.	Starting Cycle	Method	MAE (%)	RMSE (%)	MAPE (%)
B05	Cycle115 (70%)	CGKAN	0.40	0.47	0.60
		CNN	0.80	1.00	4.26
		BiGRU	0.15	0.19	0.22
		CNN-BiGRU	0.61	0.72	0.92
B06	Cycle115 (70%)	CGKAN	0.78	1.01	1.26
		CNN	0.88	1.10	1.42
		BiGRU	0.97	1.14	1.57
		CNN-BiGRU	1.12	1.46	1.88

Table 2. *Cont.*

No.	Starting Cycle	Method	MAE (%)	RMSE (%)	MAPE (%)
B07	Cycle115 (70%)	CGKAN	0.63	0.74	0.88
		CNN	0.97	1.11	1.33
		BiGRU	1.28	1.44	1.78
		CNN-BiGRU	1.09	1.38	1.52
B18	Cycle90 (70%)	CGKAN	0.66	0.85	0.96
		CNN	0.98	1.20	1.41
		BiGRU	0.81	1.02	1.15
		CNN-BiGRU	0.89	1.06	1.29
AVERAGE	70%	CGKAN	0.62	0.77	0.93
		CNN	0.91	1.10	2.11
		BiGRU	0.80	0.95	1.18
		CNN-BiGRU	0.93	1.16	1.40
B05	Cycle80 (50%)	CGKAN	0.60	0.68	0.87
		CNN	2.42	2.64	3.43
		BiGRU	0.68	0.81	0.99
		CNN-BiGRU	2.42	3.04	3.58
B18	Cycle65 (50%)	CGKAN	0.58	0.77	0.81
		CNN	1.50	1.84	2.14
		BiGRU	1.01	1.09	1.43
		CNN-BiGRU	1.25	1.48	1.80
AVERAGE	50%	CGKAN	0.59	0.73	0.84
		CNN	1.96	2.24	2.79
		BiGRU	0.85	0.95	1.21
		CNN-BiGRU	1.84	2.26	2.69

Analysis of Figure 5 and Table 2 shows that the CGKAN method outperforms other methods on the B05, B06, B07, and B18 datasets, particularly on the B06 and B18 datasets, where the average errors (MAE, RMSE, MAPE) of CGKAN are significantly lower than those of other methods. While the BiGRU method performs well on certain datasets (such as B05), its estimation accuracy decreases on other datasets, showing some instability. The performance of CNN-BiGRU is slightly worse than that of BiGRU, which may be due to a lack of generalization capability caused by increased model complexity. In contrast, CGKAN, by incorporating the efficient feature representation capability of KAN, overcomes the potential drawbacks associated with model complexity.

To investigate the impact of different starting cycle on SOH estimation performance, experiments were conducted on the B05 and B18 batteries. The estimation results and evaluation metrics are shown in Figure 5 and Table 2. As the available battery cycle data decreases, the overall performance of all methods declines. However, the performance of CGKAN does not exhibit a significant drop, and its accuracy remains relatively stable. In contrast, CNN and CNN-BiGRU show a noticeable reduction in estimation accuracy when the number of learnable samples decreases. Although BiGRU outperforms CNN and CNN-BiGRU on some metrics, it still does not surpass CGKAN. Furthermore, it is observed that for the B18 battery, when the estimation starting cycle is changed to 50%, the

estimation performance improves compared to the 70%. This improvement is due to the inclusion of cycles 65 to 80 in the test set, which are easier to learn.

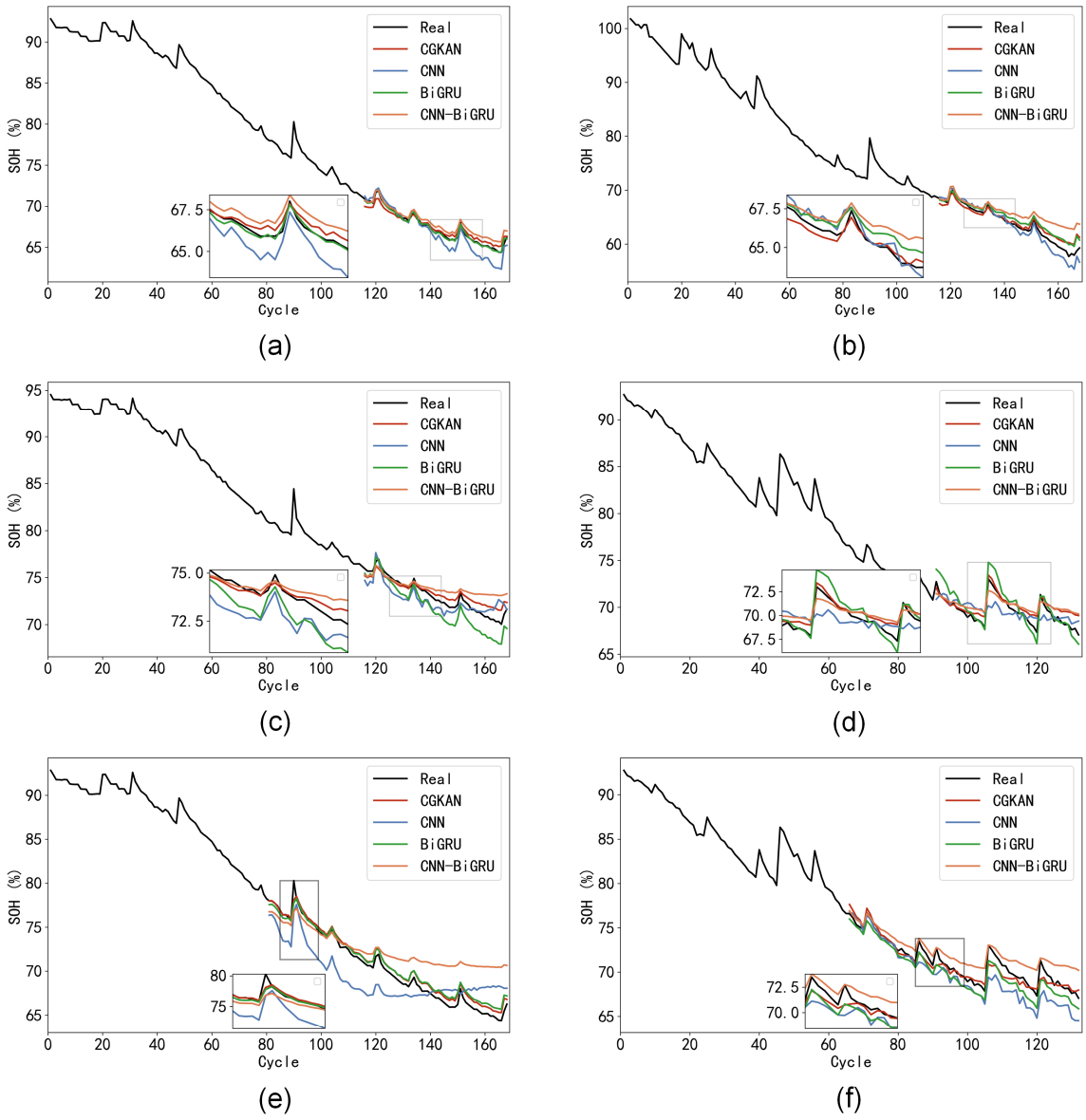


Figure 5. SOH estimation experiments on the NASA dataset: 70%Cycle: (**a**) B05; (**b**) B06; (**c**) B07; (**d**) B18, 50%Cycle: (**e**) B05; (**f**) B18.

Table 3. Evaluation metrics of ablation settings and initialization cycles on the CALCE dataset.

No.	Starting Cycle	Method	MAE (%)	RMSE (%)	MAPE (%)
CS2_35	Cycle617 (70%)	CGKAN	0.95	1.25	2.38
		CNN	1.17	1.55	2.71
		BiGRU	1.34	1.66	3.03
		CNN-BiGRU	1.30	1.68	2.89
CS2_36	Cycle655 (70%)	CGKAN	0.91	1.15	3.27
		CNN	4.28	5.71	17.51
		BiGRU	1.34	1.74	5.16
		CNN-BiGRU	2.11	2.61	7.61

Table 3. *Cont.*

No.	Starting Cycle	Method	MAE (%)	RMSE (%)	MAPE (%)
CS2_37	Cycle680 (70%)	CGKAN	1.28	1.57	3.22
		CNN	2.24	3.99	7.64
		BiGRU	1.34	2.09	4.17
		CNN-BiGRU	1.38	1.73	3.72
CS2_38	Cycle697 (70%)	CGKAN	1.26	1.53	2.50
		CNN	3.23	3.70	6.65
		BiGRU	2.59	2.99	6.30
		CNN-BiGRU	1.42	1.61	3.01
AVERAGE	70%	CGKAN	1.10	1.38	2.84
		CNN	2.73	3.74	8.63
		BiGRU	1.65	2.12	4.67
		CNN-BiGRU	1.55	1.91	4.31
CS2_35	Cycle441 (50%)	CGKAN	1.33	1.99	3.06
		CNN	2.24	2.95	4.65
		BiGRU	2.20	2.49	4.43
		CNN-BiGRU	1.72	2.66	4.09
CS2_38	Cycle498 (50%)	CGKAN	2.03	2.64	4.58
		CNN	2.68	4.00	6.44
		BiGRU	3.34	2.66	6.01
		CNN-BiGRU	3.19	4.50	7.63
AVERAGE	50%	CGKAN	1.68	2.32	3.82
		CNN	2.46	3.48	5.55
		BiGRU	2.77	2.58	5.22
		CNN-BiGRU	2.46	3.58	5.86

Based on the CALCE battery SOH estimation results (Figure 6) and evaluation metrics (Table 3), CGKAN outperforms CNN, BiGRU, and CNN-BiGRU on the longer degradation cycle CALCE dataset. CGKAN achieves an average MAE of 1.10% (reductions of 1.63%, 0.55%, and 0.45%), an average RMSE of 1.38% (reductions of 2.36%, 0.74%, and 0.53%), and an average MAPE of 2.84% (reductions of 5.79%, 1.83%, and 1.47%) compared to the other methods.

To investigate the impact of different starting cycle on SOH estimation performance, experiments were conducted using the CS2_35 and CS2_38 batteries, with 50% cycle. The SOH estimation results and evaluation metrics are shown in Figure 6 and Table 3. Analysis of the experimental results reveals that CGKAN maintains stable estimation accuracy on the CALCE dataset and significantly outperforms the CNN, BiGRU, and CNN-BiGRU methods.

To validate the advantages of the proposed method, we conducted benchmarking experiments on NASA (B18) and CALCE (CS2_38) datasets using three baselines: support vector machine (SVM) for traditional machine learning; Recurrent Neural Network (RNN); Long Short-Term Memory (LSTM) network. All models were trained on the first 70% of cycle data and tested on the rest. As shown in Figure 7 and Table 4, CGKAN outperforms the baselines in most cases, achieving the lowest RMSE on CS2_38. Although SVM performs

slightly better on B18, this is likely due to its small data size and simpler degradation trends, which favor traditional models under limited data conditions.

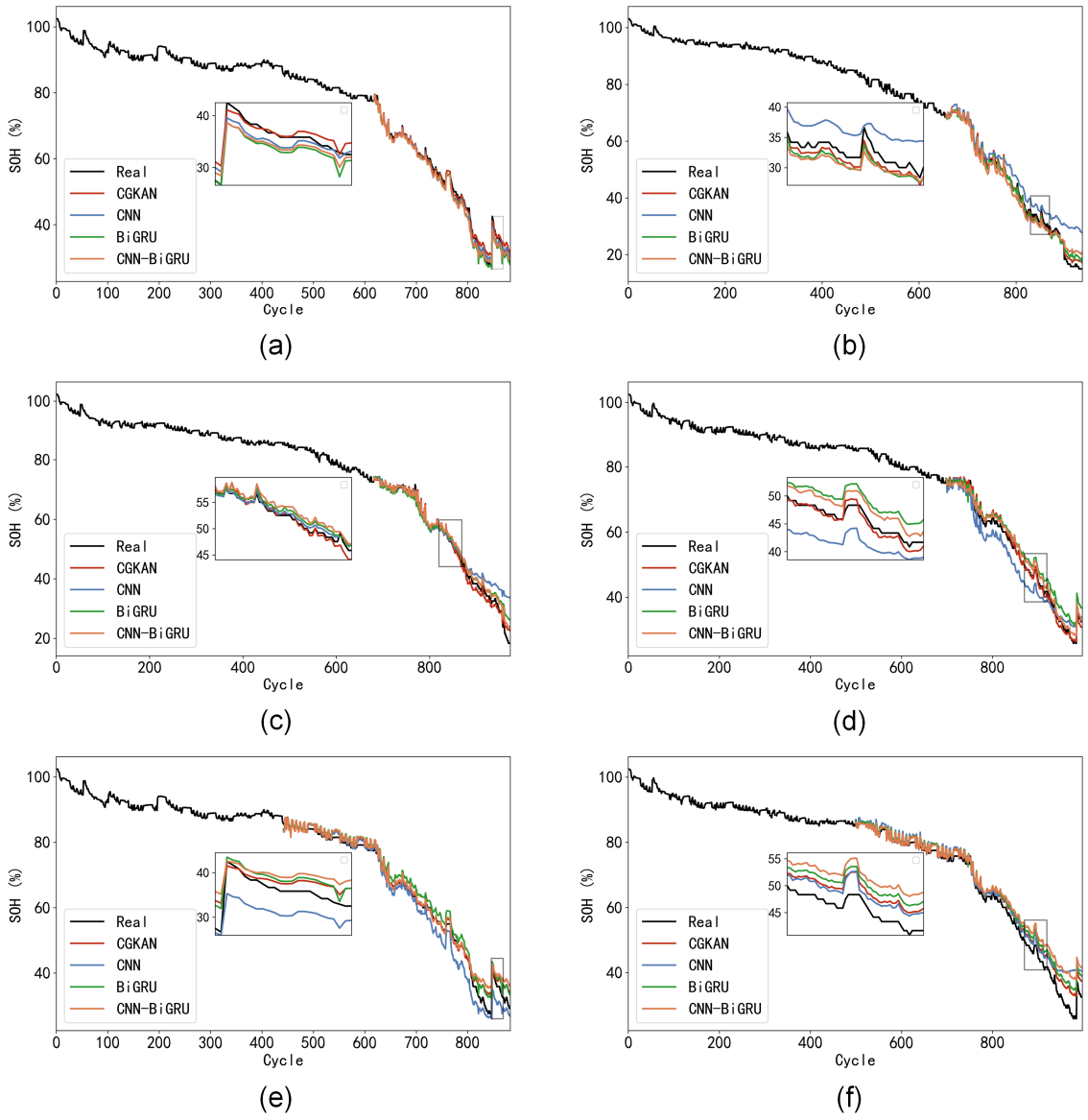


Figure 6. SOH estimation experiments on the CALCE dataset: 70%Cycle: (**a**) CS2_35; (**b**) CS2_36; (**c**) CS2_37; (**d**) CS2_38, 50%Cycle: (**e**) CS2_35; (**f**) CS2_38.

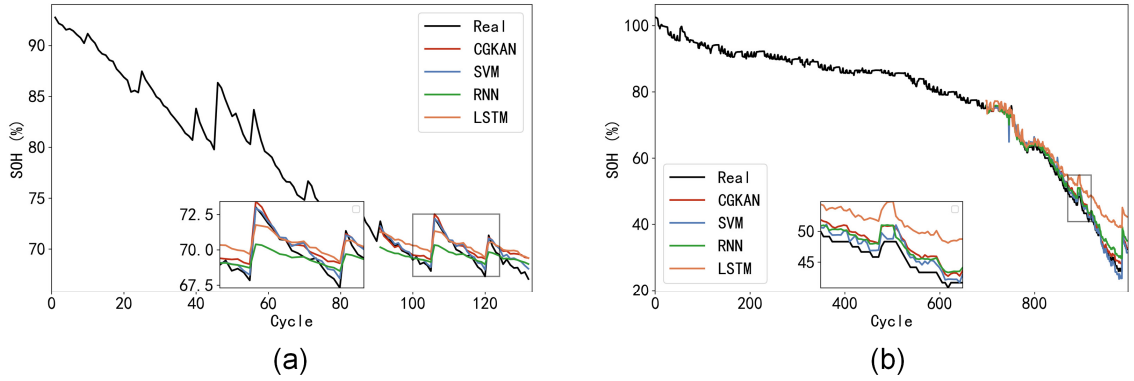


Figure 7. Estimation results of different SOH estimation methods: (**a**) B18; (**b**) CS2_38.

Table 4. Evaluation of accuracy and computational efficiency across models.

No.	Method	RMSE (%)	Parameters (M)	Model Size (MB)	FLOPs (M)
B18	CGKAN	0.66	0.16	0.67	0.51
	SVM	0.60	-	0.01	-
	RNN	1.04	0.03	0.11	0.15
	LSTM	1.14	0.08	0.32	0.43
CS2_38	CGKAN	1.26	0.16	0.67	0.51
	SVM	1.34	-	0.01	-
	RNN	1.95	0.03	0.11	0.15
	LSTM	5.06	0.08	0.32	0.43
AVERAGE	CGKAN	0.96	0.16	0.67	0.51
	SVM	0.97	-	0.01	-
	RNN	1.50	0.03	0.11	0.15
	LSTM	3.10	0.08	0.32	0.43

To further assess its practicality, Table 4 compares the computational efficiency of all models, including RMSE, parameter count, model size, and FLOPs. Despite incorporating three modules, CGKAN maintains a reasonable parameter scale and model size. CGKAN achieves substantial improvements in accuracy with only a modest increase in complexity. This highlights CGKAN's favorable trade-off between estimation performance and computational cost, supporting its potential for real-world deployment in battery health monitoring applications.

From the analysis of Figures 5–7 and Tables 2–4, it can be concluded that the CGKAN method effectively integrates the characteristics of CNN and BiGRU, while addressing the issue of insufficient global information capture in single models for time-series modeling through the KAN module. Compared to using CNN or BiGRU individually, the proposed method not only accurately captures the declining trend of battery capacity but also adapts to the capacity regeneration phenomenon during the aging process, demonstrating good generalization ability across different battery groups. Additionally, the CGKAN's favorable balance between estimation performance and computational cost makes it promising for practical deployment in battery health monitoring applications.

4.2. SOH Estimation Based on Multiple Battery Aging Information

To analyze the relationships between the aging data of multiple batteries and test the generalization ability of CGKAN throughout the entire life cycle of new batteries, this section uses arbitrary data from three batteries in the NASA and CALCE datasets as training data. The trained model is then used to estimate the SOH of a fourth battery. The SOH estimation results are shown in Figure 8, and the evaluation metrics are presented in Table 5.

As shown in Figure 8, CGKAN is able to accurately fit the complete degradation trend of new batteries in both the NASA and CALCE datasets. It is worth noting that the proposed method exhibits poorer fitting performance on CS2_36, which may be attributed to a sudden change in SOH at cycle 900. This abrupt change reflects abnormal behaviors in the actual battery operation, such as sudden aging or external environmental influences. Such mutations not only challenge the health status of the battery itself but also make the data distribution more complex and unstable. Compared to other batteries, the data of

CS2_36 exhibit stronger non-stationarity and discontinuity, particularly near the mutation point, where the SOH change trend fails to follow the previous regularity.

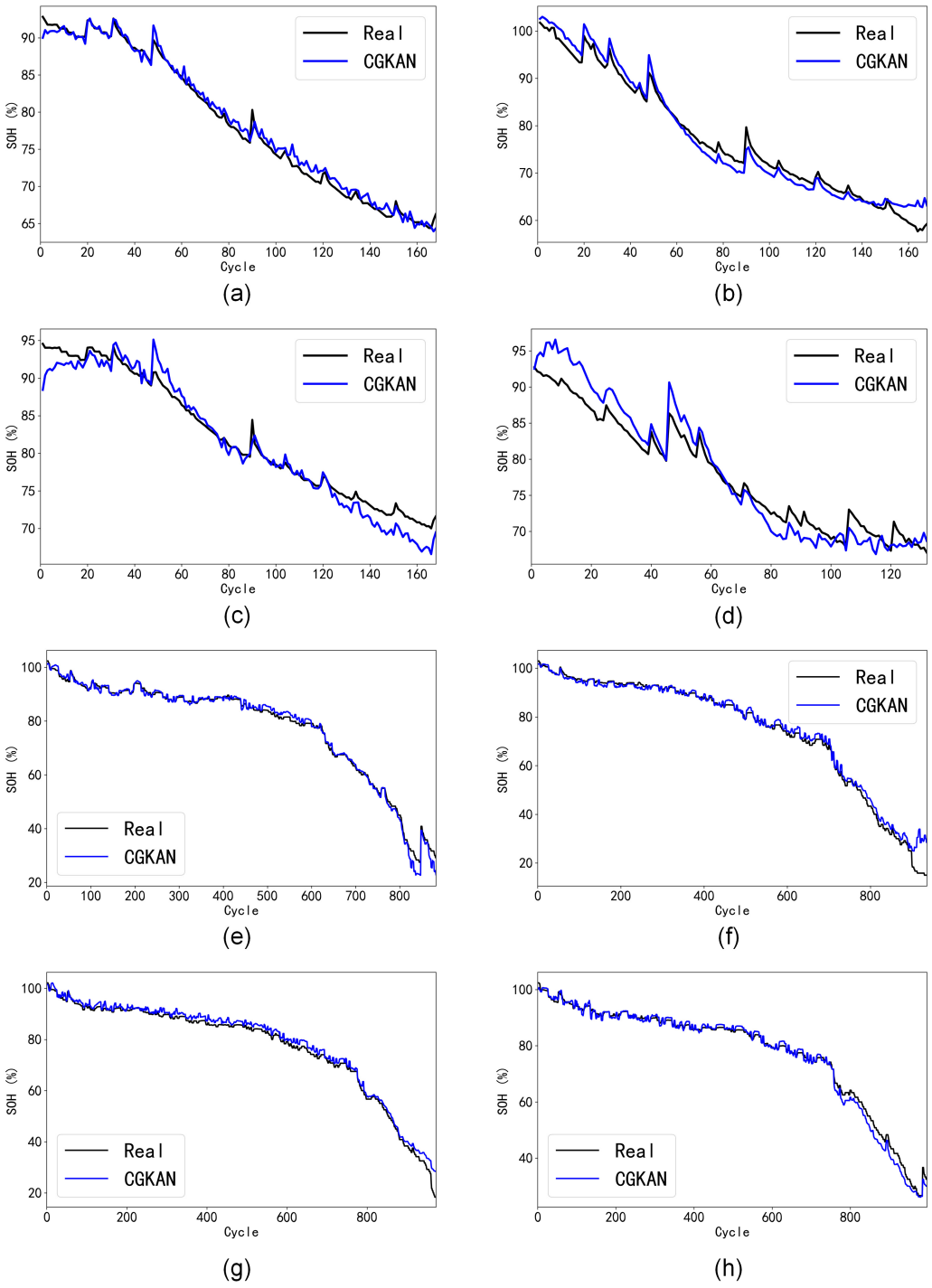


Figure 8. Estimation results based on aging information of multiple batteries: (**a**) B05; (**b**) B06; (**c**) B07; (**d**) B18; (**e**) CS2_35; (**f**) CS2_36; (**g**) CS2_37; (**h**) CS2_38.

From Table 5, it can be seen that the maximum MAE, RMSE, and MAPE for the NASA dataset are below 2.0%, 2.4%, and 2.5%, respectively, while the maximum MAE, RMSE, and MAPE for the CALCE dataset are below 1.7%, 3.0%, and 5.1%, respectively. This indicates that CGKAN has high precision and generalization ability, enabling SOH estimation for new batteries based on historical battery data. Moreover, as the data size increases, the

method can more effectively capture key degradation information of new batteries, further improving estimation accuracy.

Table 5. Evaluation metrics for new battery SOH estimation.

Training Data	Test Data	MAE (%)	RMSE (%)	MAPE (%)
B06+07+18	B05	0.70	0.90	0.92
B05+07+18	B06	1.69	1.98	2.27
B05+06+18	B07	1.30	1.68	1.61
B05+06+07	B18	2.00	2.38	2.50
CS2_36+37+38	CS2_35	1.04	1.50	1.89
CS2_35+37+38	CS2_36	1.66	2.98	5.14
CS2_35+36+38	CS2_37	1.59	1.99	2.84
CS2_35+36+37	CS2_38	1.26	1.67	2.13

4.3. SOH Estimation Experiment Under Complex Operating Conditions

Different operating conditions can directly affect the battery aging process. For example, high and low temperatures alter the rate of chemical reactions inside the battery and can damage the internal materials; high-rate discharge generates more heat within the battery, accelerating aging. To validate the estimation accuracy of the proposed method under complex conditions, the NASA batteries B34, B45, and B55 were selected for the SOH estimation experiment, with the experimental setup consistent with Section 4.1. To rigorously evaluate dynamic operating conditions, additional validation was conducted on the CALCE CS2_3 battery, which features a cyclically varying discharge current across cycles. Specifically, the discharge current increases in a six-step pattern ($0.11 \rightarrow 0.22 \rightarrow 0.55 \rightarrow 1.1 \rightarrow 1.65 \rightarrow 2.2$ A) and then repeats from 0.11 A in subsequent cycles, simulating phased load variations encountered in real-world applications. The experimental results are shown in Figure 9, and the evaluation metrics are presented in Table 6.

As shown in Figure 9, the capacity degradation curves of B34 and B55 exhibit strong nonlinearity. For instance, the B34 battery experiences significant capacity regeneration at cycle 152, yet the proposed method still performs well at this point, with the overall error controlled within 4%. For B55, the error is controlled within 3%, and for B45, the maximum error is kept within 4%. The method's robustness is further confirmed by testing on CS2_3 under current-varying conditions, where discharge current progressively increases from 0.11 A to 2.2 A across cycles (20-fold difference between minimum and maximum currents). Despite this extreme dynamic range, the estimation errors remain consistently within 6% throughout all current levels. As indicated in Table 6, although the estimation accuracy varies across each battery, the average MAE, RMSE, and MAPE for the three batteries are 0.80%, 0.99%, and 1.37%, respectively, which are close to the SOH estimation accuracy observed under milder operating conditions.

The B34 battery is selected to study the impact of using 50% as the estimation starting cycle on the model's estimation performance under complex operating conditions. The experimental results are shown in Figure 9 and Table 6.

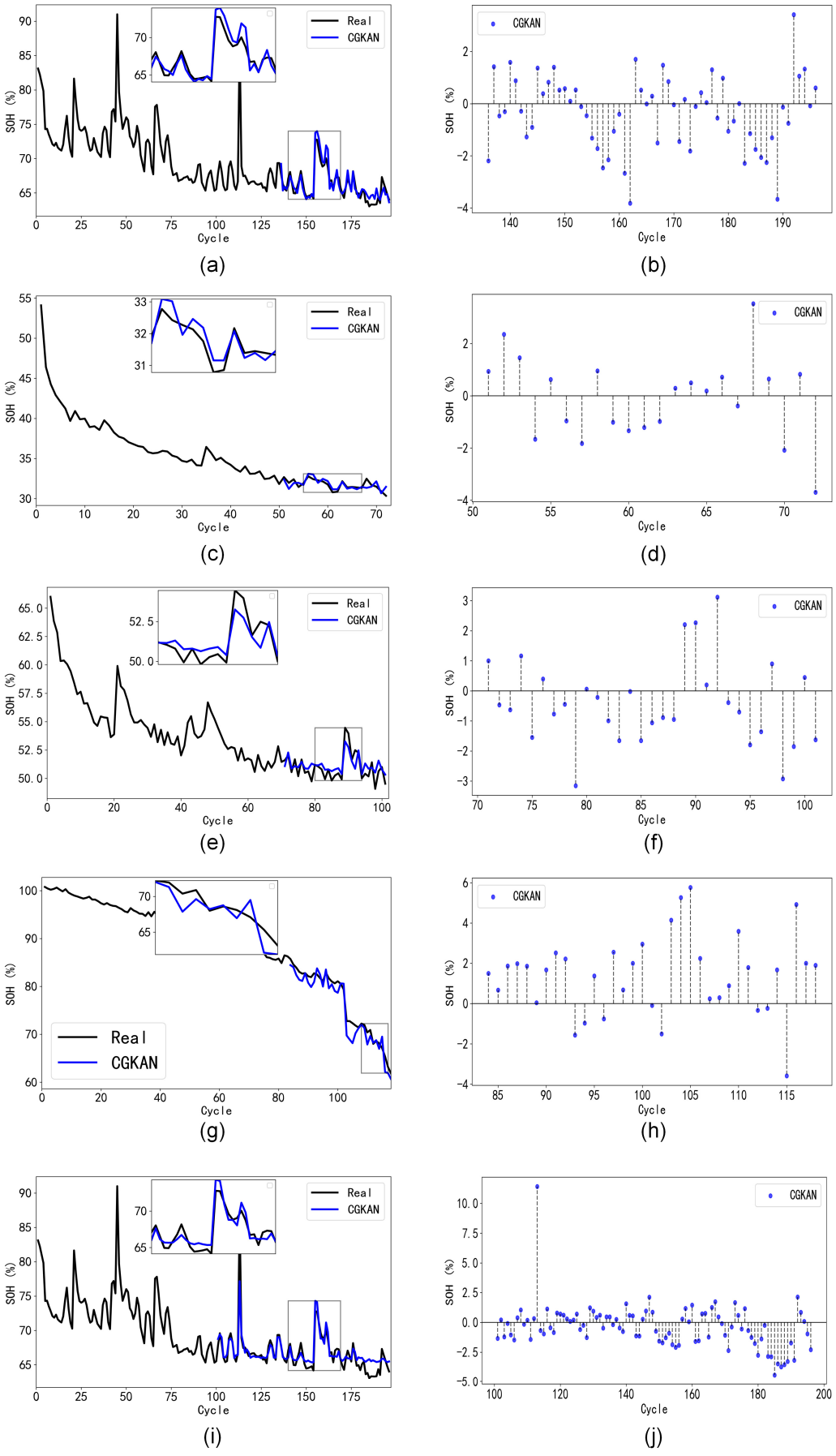


Figure 9. SOH estimation results and corresponding errors under complex conditions: B34 (**a**,**b**) and B45 (**c**,**d**), B55 (**e**,**f**), and CS2_3 (**g**,**h**) for 70% cycle; B34 (**i**,**j**) for 50% cycle.

Table 6. Evaluation metrics under complex operating conditions.

No.	Starting Cycle	MAE (%)	RMSE (%)	MAPE (%)
B34	Cycle135 (70%)	0.74	0.96	1.11
B45	Cycle50 (70%)	0.41	0.50	1.28
B55	Cycle70 (70%)	0.61	0.75	1.19
CS2_3	Cycle70 (70%)	1.45	1.77	1.93
AVERAGE	70%	0.80	0.99	1.37
B34	Cycle100 (50%)	0.86	1.39	1.26

Analysis of Figure 9 and Table 6 shows that when the starting cycle is advanced, the accuracy metrics of the proposed CGKAN method are only slightly varied. When 50% cycle is used as the estimation starting cycle, the MAE and RMSE increase by only 0.12% and 0.43%, respectively, compared to the 70%. This result indicates that the CGKAN method provides relatively accurate estimation results even with fewer known cycle data, and the average evaluation metrics remain close to those under mild conditions, further demonstrating the method's stability and adaptability.

Through the SOH estimation experiments conducted in Sections 4.1–4.3 under various batteries, temperatures, and discharge rates, the results show that the proposed method can accurately estimate battery SOH, maintaining good accuracy even under capacity regeneration or nonlinear degradation. Furthermore, even with limited available cycle data, the proposed method continues to provide stable and effective estimation results, showcasing strong adaptability and robustness.

5. Conclusions

To improve the accuracy of lithium-ion battery State of Health (SOH) estimation, this paper proposes a novel SOH estimation method based on partial discharge curves.

Firstly, considering that it is difficult to obtain full discharge data in practical applications and that the SOC range is typically from 80% to 20%, the method extracts health-related features corresponding to voltage and IC curves from partial discharge curves within this SOC range. These features are then analyzed for their importance using random forest regression, and those highly correlated with SOH are selected as the model's input.

Secondly, since CNNs can only capture local features and are limited in capturing the global trends of battery SOH, while GRUs fail to fully consider the complex nonlinear variations in battery state when modeling time-series data, this paper proposes the CGKAN method. This method utilizes CNNs to extract local features, BiGRU to capture short-term dependencies in time-series data, and KAN to provide stronger global information modeling capabilities. This combination enhances the model's ability to describe both long-term degradation and local regeneration phenomena, enabling the effective integration of local feature extraction and global information modeling to achieve high-accuracy SOH estimation.

Finally, the SOH estimation results of 11 batteries under different types and operating conditions validate that the proposed CGKAN method significantly improves estimation accuracy compared to traditional methods such as BiGRU and CNN-BiGRU. The method demonstrates stable estimation performance across different estimation start points, unknown batteries, and complex operating conditions.

Author Contributions: Conceptualization, S.H. and W.Q.; data curation, C.S.; formal analysis, Z.Y. and W.Q.; funding acquisition, Z.Y. and W.Q.; investigation, C.W.; methodology, S.H. and Z.Y.; project administration, W.Q.; resources, C.W. and C.S.; supervision, W.Q.; validation, C.W. and Z.Y.; visualization, S.H.; writing—original draft, S.H. and W.Q.; writing—review and editing, S.H. and W.Q. All authors have read and agreed to the published version of the manuscript.

Funding: This work was supported by the Key R&D Program of Jiangsu Province under Grant BE2023010-3, Jiangsu Modern Agricultural Industry Single Technology Research and Development project under Grant CX(23)3120, Advanced Computing and Intelligent Engineering (National Level) Laboratory Fund and National Key Laboratory of Ship Structural Safety Fund and the National Natural Science Foundation of China (NSFC) (52367025).

Data Availability Statement: The raw data supporting the conclusions of this article will be made available by the authors on request.

Conflicts of Interest: The authors declare no conflicts of interest.

References

1. Song, L.; Zhang, K.; Liang, T.; Han, X.; Zhang, Y. Intelligent State of Health Estimation for Lithium-Ion Battery Pack Based on Big Data Analysis. *J. Energy Storage* **2020**, *32*, 101836. [CrossRef]
2. Hu, X.; Zhang, K.; Liu, K.; Lin, X.; Dey, S.; Onori, S. Advanced Fault Diagnosis for Lithium-Ion Battery Systems: A Review of Fault Mechanisms, Fault Features, and Diagnosis Procedures. *IEEE Ind. Electron. Mag.* **2020**, *14*, 65–91. [CrossRef]
3. Sui, X. *Robust State of Health Estimation for Lithium-Ion Batteries Using Machines Learning*; Aalborg University: Aalborg, Denmark, 2021.
4. Wu, J.; Cui, X.; Meng, J.; Peng, J.; Lin, M. Data-Driven Transfer-Stacking Based State of Health Estimation for Lithium-Ion Batteries. *IEEE Trans. Ind. Electron.* **2023**, *71*, 604–614. [CrossRef]
5. Li, Q.; Li, D.; Zhao, K.; Wang, L.; Wang, K. State of Health Estimation of Lithium-Ion Battery Based on Improved Ant Lion Optimization and Support Vector Regression. *J. Energy Storage* **2022**, *50*, 104215. [CrossRef]
6. Lyu, C.; Lai, Q.; Ge, T.; Yu, H.; Wang, L.; Ma, N. A Lead-Acid Battery's Remaining Useful Life Prediction by Using Electrochemical Model in the Particle Filtering Framework. *Energy* **2017**, *120*, 975–984. [CrossRef]
7. Hu, X.; Li, S.; Peng, H. A Comparative Study of Equivalent Circuit Models for Li-Ion Batteries. *J. Power Sources* **2012**, *198*, 359–367. [CrossRef]
8. Wang, Y.; Tian, J.; Sun, Z.; Wang, L.; Xu, R.; Li, M.; Chen, Z. A Comprehensive Review of Battery Modeling and State Estimation Approaches for Advanced Battery Management Systems. *Renew. Sustain. Energy Rev.* **2020**, *131*, 110015. [CrossRef]
9. Xiong, R.; Li, L.; Li, Z.; Yu, Q.; Mu, H. An Electrochemical Model Based Degradation State Identification Method of Lithium-Ion Battery for All-Climate Electric Vehicles Application. *Appl. Energy* **2018**, *219*, 264–275. [CrossRef]
10. Deng, Z.; Hu, X.; Lin, X.; Xu, L.; Li, J.; Guo, W. A Reduced-Order Electrochemical Model for All-Solid-State Batteries. *IEEE Trans. Transp. Electrif.* **2020**, *7*, 464–473. [CrossRef]
11. Galeotti, M.; Cinà, L.; Giammanco, C.; Cordiner, S.; Di Carlo, A. Performance Analysis and SOH (State of Health) Evaluation of Lithium Polymer Batteries through Electrochemical Impedance Spectroscopy. *Energy* **2015**, *89*, 678–686. [CrossRef]
12. Hu, X.; Yuan, H.; Zou, C.; Li, Z.; Zhang, L. Co-Estimation of State of Charge and State of Health for Lithium-Ion Batteries Based on Fractional-Order Calculus. *IEEE Trans. Veh. Technol.* **2018**, *67*, 10319–10329. [CrossRef]
13. Li, J.; Adewuyi, K.; Lotfi, N.; Landers, R.; Park, J. A Single Particle Model with Chemical/Mechanical Degradation Physics for Lithium Ion Battery State of Health (SOH) Estimation. *Appl. Energy* **2018**, *212*, 1178–1190. [CrossRef]
14. Chen, S.-Z.; Liang, Z.; Yuan, H.; Yang, L.; Xu, F.; Zhang, Y. Li-Ion Battery State-of-Health Estimation Based on the Combination of Statistical and Geometric Features of the Constant-Voltage Charging Stage. *J. Energy Storage* **2023**, *72*, 108647. [CrossRef]
15. Fezai, R.; Abodayeh, K.; Mansouri, M.; Nounou, H.; Nounou, M. Fault Diagnosis of Biological Systems Using Improved Machine Learning Technique. *Int. J. Mach. Learn. Cybern.* **2021**, *12*, 515–528. [CrossRef]
16. Gou, B.; Xu, Y.; Feng, X. An Ensemble Learning-Based Data-Driven Method for Online State-of-Health Estimation of Lithium-Ion Batteries. *IEEE Trans. Transp. Electrif.* **2020**, *7*, 422–436. [CrossRef]
17. Teng, J.-H.; Chen, R.-J.; Lee, P.-T.; Hsu, C.-W. Accurate and Efficient SOH Estimation for Retired Batteries. *Energies* **2023**, *16*, 1240. [CrossRef]
18. Pan, H.; Lü, Z.; Wang, H.; Wei, H.; Chen, L. Novel Battery State-of-Health Online Estimation Method Using Multiple Health Indicators and an Extreme Learning Machine. *Energy* **2018**, *160*, 466–477. [CrossRef]
19. Zhu, J.; Wang, Y.; Huang, Y.; Bhushan Gopaluni, R.; Cao, Y.; Heere, M.; Mühlbauer, M.J.; Mereacre, L.; Dai, H.; Liu, X.; et al. Data-Driven Capacity Estimation of Commercial Lithium-Ion Batteries from Voltage Relaxation. *Nat. Commun.* **2022**, *13*, 2261. [CrossRef]

20. Weng, C.; Sun, J.; Peng, H. Model Parametrization and Adaptation Based on the Invariance of Support Vectors with Applications to Battery State-of-Health Monitoring. *IEEE Trans. Veh. Technol.* **2014**, *64*, 3908–3917. [CrossRef]
21. Wang, Z.; Yuan, C.; Li, X. Lithium Battery State-of-Health Estimation via Differential Thermal Voltammetry with Gaussian Process Regression. *IEEE Trans. Transp. Electrif.* **2020**, *7*, 16–25. [CrossRef]
22. Wu, M.; Zhong, Y.; Wu, J.; Wang, Y.; Wang, L. State of Health Estimation of the Lithium-Ion Power Battery Based on the Principal Component Analysis-Particle Swarm Optimization-Back Propagation Neural Network. *Energy* **2023**, *283*, 129061. [CrossRef]
23. Yun, Z.; Qin, W.; Shi, W.; Ping, P. State-of-Health Prediction for Lithium-Ion Batteries Based on a Novel Hybrid Approach. *Energies* **2020**, *13*, 4858. [CrossRef]
24. Yang, N.; Song, Z.; Hofmann, H.; Sun, J. Robust State of Health estimation of lithium-ion batteries using convolutional neural network and random forest. *J. Energy Storage* **2022**, *48*, 103857. [CrossRef]
25. Zheng, Y.; Hu, J.; Chen, J.; Deng, H.; Hu, W. State of health estimation for lithium battery random charging process based on CNN-GRU method. *Energy Rep.* **2023**, *9*, 1–10. [CrossRef]
26. Wang, X.; Hu, B.; Su, X.; Xu, L.; Zhu, D. State of Health estimation for lithium-ion batteries using Random Forest and Gated Recurrent Unit. *J. Energy Storage* **2024**, *76*, 109796. [CrossRef]
27. Saha, B.; Goebel, K. *Battery Data Set*; NASA Prognostics Data Repository, NASA Ames Research Center: Moffett Field, CA, USA, 2007. Available online: https://www.nasa.gov/intelligent-systems-division/discovery-and-systems-health/pcoe/pcoe-data-set-repository/ (accessed on 10 February 2025).
28. CALCE Battery Research Group of the University of Maryland. Battery Data Set. Available online: https://calce.umd.edu/battery-data (accessed on 10 February 2025).
29. Goebel, K.; Saha, B.; Saxena, A.; Celaya, J.R.; Christophersen, J.P. Prognostics in Battery Health Management. *IEEE Instrum. Meas. Mag.* **2008**, *11*, 33–40. [CrossRef]
30. He, W.; Williard, N.; Osterman, M.; Pecht, M. Prognostics of Lithium-Ion Batteries Based on Dempster–Shafer Theory and the Bayesian Monte Carlo Method. *J. Power Sources* **2011**, *196*, 10314–10321. [CrossRef]
31. Jia, Q.-S.; Long, T. A Review on Charging Behavior of Electric Vehicles: Data, Model, and Control. *Control Theory Technol.* **2020**, *18*, 217–230. [CrossRef]
32. Xu, J.; Liu, B.; Zhang, G.; Zhu, J. State-of-health Estimation for Lithium-ion Batteries Based on Partial Charging Segment and Stacking Model Fusion. *Energy Sci. Eng.* **2023**, *11*, 383–397. [CrossRef]
33. Lin, M.; Wu, D.; Meng, J.; Wu, J.; Wu, H. A Multi-Feature-Based Multi-Model Fusion Method for State of Health Estimation of Lithium-Ion Batteries. *J. Power Sources* **2022**, *518*, 230774. [CrossRef]
34. Zhi, Y.; Wang, H.; Wang, L. A State of Health Estimation Method for Electric Vehicle Li-Ion Batteries Using GA-PSO-SVR. *Complex Intell. Syst.* **2022**, *8*, 2167–2182. [CrossRef]
35. Breiman, L. Random Forests. *Mach. Learn.* **2001**, *45*, 5–32. [CrossRef]
36. Firsov, N.; Myasnikov, E.; Lobanov, V.; Khabibullin, R.; Kazanskiy, N.; Khonina, S.; Butt, M.A.; Nikonorov, A. HyperKAN: Kolmogorov–Arnold Networks Make Hyperspectral Image Classifiers Smarter. *Sensors* **2024**, *24*, 7683. [CrossRef]
37. Livieris, I.E. C-KAN: A New Approach for Integrating Convolutional Layers with Kolmogorov–Arnold Networks for Time-Series Forecasting. *Mathematics* **2024**, *12*, 3022. [CrossRef]
38. Kolmogorov, A.N. *On the Representation of Continuous Functions of Several Variables by Superpositions of Continuous Functions of a Smaller Number of Variables*; American Mathematical Society: Providence, RI, USA, 1961.
39. Liu, Z.; Wang, Y.; Vaidya, S.; Ruehle, F.; Halverson, J.; Soljačić, M.; Hou, T.Y.; Tegmark, M. Kan: Kolmogorov-arnold networks. *arXiv* **2024**, arXiv:2404.19756.

Disclaimer/Publisher's Note: The statements, opinions and data contained in all publications are solely those of the individual author(s) and contributor(s) and not of MDPI and/or the editor(s). MDPI and/or the editor(s) disclaim responsibility for any injury to people or property resulting from any ideas, methods, instructions or products referred to in the content.